LAWRENCE
LIVERMORE
NATIONAL
LABORATORY

LLNL-JRNL-463114

Electron heat transport from stochastic felds in gyrokinetic simulations

E. Wang, W. M. Nevins, J. Candy, D. Hatch, P. Terry, W. Guttenfelder

November 24, 2010

Physics of Plasmas

Disclaimer

This document was prepared as an account of work sponsored by an agency of the United States government. Neither the United States government nor Lawrence Livermore National Security, LLC, nor any of their employees makes any warranty, expressed or implied, or assumes any legal liability or responsibility for the accuracy, completeness, or usefulness of any information, apparatus, product, or process disclosed, or represents that its use would not infringe privately owned rights. Reference herein to any specific commercial product, process, or service by trade name, trademark, manufacturer, or otherwise does not necessarily constitute or imply its endorsement, recommendation, or favoring by the United States government or Lawrence Livermore National Security, LLC. The views and opinions of authors expressed herein do not necessarily state or reflect those of the United States government or Lawrence Livermore National Security, LLC, and shall not be used for advertising or product endorsement purposes.

LLNL-JRNL-463114

Electron heat transport from stochastic fields in gyrokinetic simulations

E. Wang and W.M. Nevins
Lawrence Livermore National Laboratory,
7000 East Ave L-637, Livermore, CA 94550

J. Candy
General Atomics, P.O. Box 85608, San Diego, CA 92186-5608, USA

D. Hatch and P. Terry
University of Wisconsin, Madison, 1150 University Avenue Madison, WI 53706-1390

W. Guttenfelder
Princeton Plasma Physics Laboratory,
P.O. Box 451, Princeton, NJ 08543

(Dated: March 3, 2011)

Abstract

GYRO is used to examine the perturbed magnetic field structure generated by electromagnetic gyrokinetic simulations of the CYCLONE base case as β_e is varied from 0.1% to 0.7%, as investigated in [J. Candy, Phys. Plasmas **12**, 072307 (2005)]. Poincare surface of section plots obtained from integrating the self-consistent magnetic field demonstrate widespread stochasticity for all nonzero values of β_e. Despite widespread stochasticity of the perturbed magnetic fields, no significant increase in electron transport is observed. The magnetic diffusion, d_m [A.B. Rechester and M.N. Rosenbluth, PRL **40**, 38 (1978)] is used to quantify the degree of stochasticity, and related to the electron heat transport for hundreds of time slices in each simulation.

INTRODUCTION

One of the fundamental components of a steady state tokamak or stellerator fusion reactor is the integrity of nested magnetic surfaces. Loss of these magnetic surfaces can have very serious implications, ranging from sawtooth crashes to disruptions. A mechanism for destroying surfaces is electromagnetic instabilities. Gyrokinetic simulation codes are now capable of modeling plasma microturbulence including kinetic ions, electrons and electromagnetic effects [1–4], allowing for study of magnetic surface integrity in the presence of the perturbed magnetic field. Gyrokinetic simulations including kinetic ions and electromagnetic effects [2, 5, 6] were done about the CYCLONE [7] base case operating point. The strength of electromagnetic effects is quantified by the electron $\beta_e = 8\pi n_e T_e/B^2$, where n_e and T_e are the equilibrium electron density and temperature, and B is the magnitude of the magnetic field. For plasmas with equal ion and electron temperatures, $2\beta_e = \beta = 8\pi p/B^2$, where p is the total plasma pressure. In the following analysis, β_e is varied from zero to 0.7% about the CYCLONE base case. The behavior of gyrokinetic simulations about CYCLONE for β_e values beyond what is presented here is the subject of ongoing study [8, 9], and not in the scope of what will be presented. For reference, the ideal MHD β-limit for this simulation is $\beta_e \sim 1.5\%$ under the artificial assumption $\alpha_{MHD} = 0$, as detailed in Reference [5].

Figure 1 demonstrates the relative magnitude of ion and electron heat flux over the range of the β_e scan run with GYRO. The electron transport is divided into electrostatic and electromagnetic components, where the electrostatic component results from the radial component of $E \times B$ drifts and the electromagnetic component represents the radial motion of electrons caused by streaming along the total magnetic field (equilibrium plus perturbations). The ion diffusivity is almost entirely electrostatic because the dominant instability with CYCLONE parameters is the ion temperature gradient (ITG) instability. A physical explanation for the drop in ion transport with increasing β_e can be understood as β_e stabilizing the ITG instability by diverting energy into bending the field line [10]. Over the range of β_e studied, the magnetic flutter component of electron transport increases from effectively zero to a fifth of the total transport or about 30% of the electron transport. The CYCLONE base case parameters are $R_0/a = 2.775$, $r/a = 0.5$, $T_e = T_i$, $R_0/L_{Te} = R_0/L_{Ti} = 6.99$, $R_0/L_n = 2.2$, $q = 1.4$, $s = 0.786$, and $\nu_{ei} = 0$. R_0 and a are the major and minor radii of the tokamak, T_e and T_i are the equilibrium electron and ion temperature, the temperature and

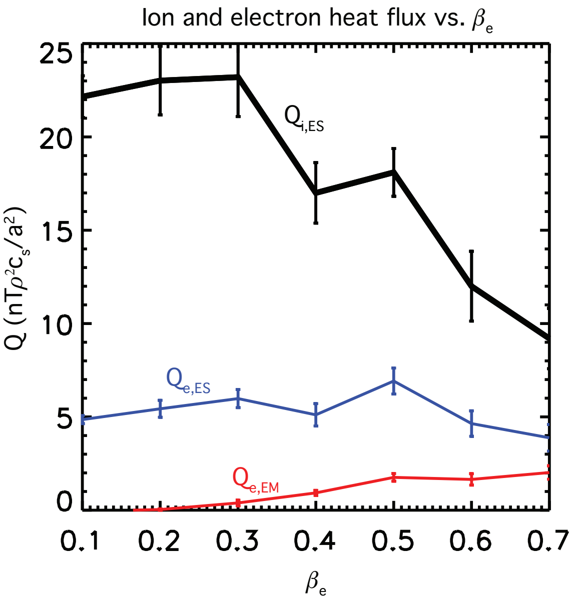

FIG. 1. (Color online) Ion (black), electron electrostatic (blue) and electron electromagnetic (red) heat flux vs β_e. Time averages are taken between $t = 150c_s/a$ and $t = 500c_s/a$.

density gradient length scales are defined as $L_{Te} = (dlnT_e/dr)^{-1}$ and $L_{Ne} = (dlnN_e/dr)^{-1}$, q is the magnetic safety factor with the magnetic shear $s = (r/q)\partial q/\partial r$, and ν_{ei} is the electron-ion collision frequency normalized to c_s/a where the sound speed $c_s = \sqrt{T_e/m_i}$. The CYCLONE geometry is a circular s-α geometry, with $\alpha = q^2Rd\beta/dr$ set to zero. In addition to varying β_e, we also use kinetic electrons with mass ratio $\mu = \sqrt{m_i/m_e} = 42$. This choice of mass ratio corresponds to a hydrogen plasma as opposed to deuterium, and matches the value chosen in References [3, 5]

GYRO employs a fieldline following coordinate system using spatial variables (ψ, θ, α), and the Clebsch representation [11] for the magnetic field $B_0 = \nabla\alpha \times \nabla\psi$. The coordinate ψ, equal to the poloidal flux divided by 2π in general gemoetries, is related the midplane minor radius r for circular geometries. The fieldline label α relates to toroidal angle ϕ by $\alpha = \phi + v(r, \theta)$. Because r and α label field lines in the Clebsh representation, θ is both the poloidal angle and the position along a fieldline labeled by remaining coordinates (r, α). The velocity grid of the presented data consists of 128 points (8 energies,8 pitch angles, and 2 signs of velocity). The spatial grid consists of 14 parallel gridpoints for each sign of velocity, 120 radial gridpoints and $k_\perp\rho_s$ values are (0,0.084,0.168,...,1.26) for a total of 16 toroidal modes. We use $k_\perp$ to represent the component of the wavenumber in the direction perpendicular to both $\nabla\psi$ and magnetic field unit vector $\mathbf{b} = \mathbf{B}/B$. The sound radius $\rho_s = (m_i T_e)^{1/2}/eB$ with e being the magnitude of the charge on an electron.

Recent work on this β_e scan of the CYCLONE base case demonstrates widespread breaking of the magnetic fieldlines even at the lowest nonzero value of β_e [12]. The authors find that the broken surfaces do not result in a dramatic rise and transport, and use the magnetic diffusion coefficient [13] to describe observed levels of electron transport. Here, we expand on the results of [12] in several ways. We emphasize that the reconnection must be driven nonlinearly, that the stochastic structure is a consequence of interaction of islands of different order and extend the analysis beyond the CYCLONE base case to a simulation where the microtearing mode is the dominant instability. The paper is organized as follows. In Section 2, we give a criterion (the resonance condition) for magnetic reconnection and demonstrate that it is satisfied for the lowest value of β_e in the CYCLONE scan. Upon observing reconnection, we produce Poincaré surface of section plots to analyze the structure of the field, and demonstrate both that the field is stochastic and the stochasticity must be caused by interaction of islands of differing order. In Section 3, we demonstrate a quantitative relation between the Rechester and Rosenbluth magnetic diffusion coefficient [13] and electron heat transport. The predictions of electron heat flux are compared to output from GYRO, and this model is then applied to a simulation where the microtearing mode is the dominant instability.

RECONNECTION AND STOCHASTICITY

In GYRO, the magnetic potential $A_\parallel$ is decomposed into Fourier harmonics given by

$$A_\parallel(r,\theta,\phi) = \sum_{j=N+1}^{j=N-1} A_{\parallel n}(r,\theta)\exp^{-in\alpha}, \tag{1}$$

with $n = j\Delta n$. To ensure $A_\parallel$ is real, only $n_n = N+1$ complex modes $j = 0, \cdots, N$ are kept in the simulation with the requirement $A^*_{\parallel n} = A_{\parallel -n}$ for the negative j counterparts. $A_\parallel$ then causes magnetic reconnection if it satisfies the resonance condition [15], $m = nq(r)$. Here, n is the toroidal mode number and m is the poloidal mode number. In effect, this condition determines the radial locations where the magnetic potential $A_\parallel(n)$ is resonant. Because gyrokinetic simulations have discrete toroidal mode numbers, the resonance condition is satisfied at discrete radial locations determined by the safety factor

$$q(r) = m/n \approx q_0[1 - s(r - r_0)/r_0]. \tag{2}$$

The center of the simulation $r_0 = .5a$ is where the safety factor $q_0 = 1.4$. The minimum n value in the simulation is 12, with all other values of n being integer multiples of the minimum value. Because the smallest n value is quite large, we note that any reconnection observed must be caused by higher order islands- the lowest order resonant rational surfaces in the simulation domain are $14/12, 15/12, 16/12$ and $17/12$. The radial locations corresponding to these values are found using Equation 2 with $n = 12$.

Once the radial locations of resonances have been determined, the proper toroidal mode number m must be singled out. This amounts to requiring $A_{\|}$ to have a nonzero average parallel to the field at the rational surface locations $r = r_{rat}(n)$. In GYRO, it is equivalent to find the resonant component of $A_{\|}$ by considering the parity of the magnetic potential with θ. Modes even in θ can be resonant while odd modes cannot. The most unstable mode in CYCLONE, ITG, is driven by the electrostatic component of the perturbed fields, having even parity in electrostatic potential Φ along the field line. The linear gyrokinetic/Maxwell equations couples ϕ to $A_{\|}$ with the opposite parity along B. The unstable ITG mode in CYCLONE base case has even parity in ϕ,coupling to odd (ballooning) parity in $A_{\|}$. The fieldline average of the odd parity $A_{\|}$ must vanish. Hence, any reconnection observed in our CYCLONE base-case simulations must be nonlinearly driven. An analysis of the parallel mode structure of eigenmodes in CYCLONE (ITG as well as damped modes) in relation to tearing parity is presented in [16].

As described in [12], nonlinear simulations do in fact cause reconnection. The resonant (even parity in θ) component of the magnetic potential can be obtained by taking the θ average $\delta A_{\|}$. The q profile in CYCLONE combined with the toroidal mode number resolution will determine the radial positions of rational surfaces.

$$A_{\|}^{res} = \left\langle A_{\|}(r = r_{rat}, n, \theta) \right\rangle_{\theta}. \tag{3}$$

Figure 2 displays the resonant component of $A_{\|}(n = 12)$ versus radius and time for $\beta_e = .1\%$ on a log scale. The lines located at $r = 2.97\rho_s$, $17.86\rho_s$, $32.74\rho_s$ and $47.62\rho_s$

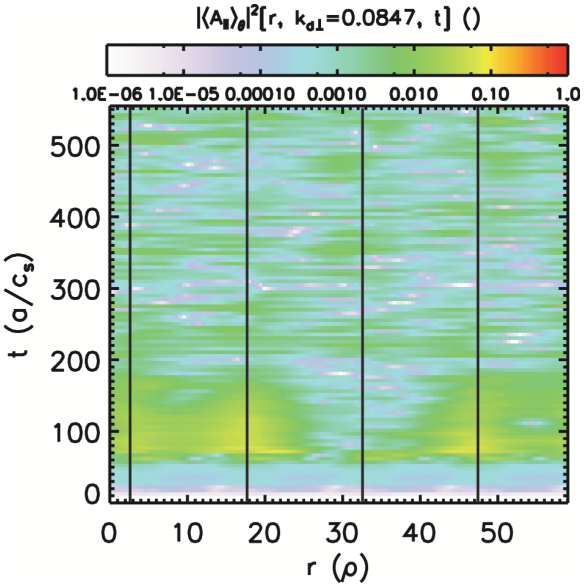

FIG. 2. (Color online) Resonant intensity of magnetic potential vs radius and time. Vertical lines are rational surface locations

are the rational surface locations of the fundamental mode ($n = 12$ or $k_\perp \rho_s = .087$) in the simulation. Because the allowed toroidal mode numbers in GYRO are integer multiples of the fundamental, the four radial locations listed are rational surfaces for all modes in the simulation. The fact that the intensity does not vanish on rational surface locations ensures that reconnection has occured, even at the lowest value of β_e simulated. What we cannot tell from Figure 2 is what type of reconnection occurs. Depending on the strength of the perturbation, islands created by reconnection may be large enough to overlap with neighboring islands causing stochasticity [14] or be small enough to be isolated from each other. Should the answer be widespread stochasticity, electrons would be free to travel across magnetic surfaces by parallel streaming and would raise significant concerns for the electron heat conductivity.

One tool to analyze how the reconnection is manifested is Poincaré surface of section plots. Surface of section plots are created by tracking the trajectory of a magnetic fieldline (r_0, α_0) and recording updated values (r_i, α_i) each time the fieldline crosses the outboard midplane. With the Clebsch representation, unperturbed fieldline trajectories are very straightforward to lowest order in gyrokinetic expansion:

$$\frac{d\psi}{d\ell} = \frac{1}{B}\mathbf{B}\cdot\nabla\psi \approx \frac{1}{B}\mathbf{B}_0\cdot\nabla\psi = 0, \tag{4}$$

$$\frac{d\alpha}{d\ell} = \frac{1}{B}\mathbf{B}\cdot\nabla\alpha \approx \frac{1}{B}\mathbf{B}_0\cdot\nabla\alpha = 0, \tag{5}$$

$$\frac{d\theta}{d\ell} = \frac{1}{B}\mathbf{B}\cdot\nabla\theta = \frac{1}{J_\psi B}, \tag{6}$$

where the Jacobian J_ψ is defined as

$$J_\psi = \frac{1}{(\nabla\alpha\times\nabla\psi)\cdot\nabla\theta}. \tag{7}$$

These equations serve to define ℓ, the distance travelled along a field line. For the circular flux-surface magnetic geometry employed in our simulations $\Delta\ell = 2\pi qR$ for one full poloidal circuit $\Delta\theta = 2\pi$. Equations 4, 5 and 6 demonstrate that without magnetic perturbations, the fieldline labels ψ and α do not evolve. The equilibrium fieldlines are periodic in coordinates (ϕ, θ), but θ is NOT periodic in coordinates (α, θ), where GYRO simulations typically cover a partial torus with toroidal domain $0 \leq \phi \leq 2\pi/\Delta n$. To account for the change in α over a full integration in θ, the the fieldline lables α_+ at $\theta = \pi$ and α_- at $\theta = -\pi$ are related by

$$\alpha_- = \alpha_+ + 2\pi q, \tag{8}$$

consistent with the partial torus domain. Accordingly, integrating from $\theta = \pi$ to $\theta = -\pi$ causes $\alpha \to \alpha + 2\pi q$. This represntation of α is periodic over the partial toroidal domain, providing a rule for mapping alpha back into the interval $-\pi\Delta n < \alpha < \pi\Delta n$.

The perturbed magnetic field $\delta\mathbf{B}$ is given by $\delta B = \nabla\times(A_\parallel\mathbf{b}) \approx (\nabla A_\parallel)\times\mathbf{b}$. Inserting this into Equations 4 and 5 we find, at first order in ρ/R, that the perturbed field line trajectories are given by

$$\frac{\partial\alpha}{\partial\ell} = \frac{\partial A_\parallel}{\partial\psi}, \frac{\partial\psi}{\partial\ell} = -\frac{\partial A_\parallel}{\partial\alpha}. \tag{9}$$

The prescription for producing a Poincaré plot consists of integrating Equation 9 over $-\pi qR \leq \ell \leq \pi qR$ from initial coordinates (r_0, α_0) to obtain new coordinates (r_1, α_1). The new value of α_1 is then modified by $2\pi q(r)$ to account for Equation 8. Final coordinates (r_1, α_1) are recorded and given a dot on a plot with x axis r and y axis α, and the integration procedure is repeated to produce (r_2, α_2), and hence a new dot. All Poincaré plots in the present paper were created using 100 initial conditions with each initial condition followed 3000 revolutions in θ. The initial conditions run diagonally through the map, starting with $r = 0, \alpha = -\pi$ up to roughly $r = 58, \alpha = \pi$.

Figure 3 demonstrates that the magnetic surfaces are destroyed for even the lowest value of β_e. Islands of stability are larger and more prevalent for the $\beta_e = .1\%$ compared with $\beta_e = .7\%$. The chaotic fieldlines are surprising to see because the magnetic component of electron heat flux is very near zero in the low β_e case. It is intructive to compare the width of magnetic islands to the separation between rational surface locations to understand why the surfaces are destroyed.

$$w_{island} = 4\sqrt{\frac{qR}{sB}|A_{\|}|}, \tag{10}$$

$$w_{separation} = \frac{1}{k_\perp s}. \tag{11}$$

Equation 11 defines the radial separation between resonant rational surfaces corresponding to a fixed $k_\perp \rho_s$. If the width of an island created is larger than the distance to the next island, the field structure will be chaotic [14]. Using Equations 10 and 11, we see the intensity of $A_\|(k_\theta)$ is not large enough to create an island of a given $k_\perp \rho$ whose width is larger than the separation between resonant surfaces $1/k_\perp s$ for all values of β_e and $k_\perp \rho_s$ (Figure 4). However, this interpretation ignores the fact that island overlap can occur between resonances of different order. Because all toroidal modes are integer multiples of the fundamental $n_0 = 12$, the minimum radial separation w_{min} between a resonance arising from n and $n + 12$ is much smaller than the separation of resonances for a fixed n.

$$w_{min} \approx \frac{\Delta k_\perp}{k_\perp^2 s}, \tag{12}$$

where $\Delta k_\perp \rho_s = 0.084$ is the increment between neighboring values of $k_\perp \rho$. The green line in Figure 4 is Equation 12, and indicates that island overlap occurs between adjacent modes at higher perpendicular modes. Figure 5 explores this phenomenon. The leftmost column is the surface of section plot using Equation 9 using only $A(k_\perp \rho = 0.084)$, or the lowest allowed value of n in Equation 1 for the integration. The second column is created by keeping the first two modes of the system, $A(k_\perp \rho = 0.084) + A(k_\perp \rho = 0.168)$, while the third and fourth columns also include $A(k_\perp \rho = 0.252)$ and $A(k_\perp \rho = 0.252) + A(k_\perp \rho = 0.336)$

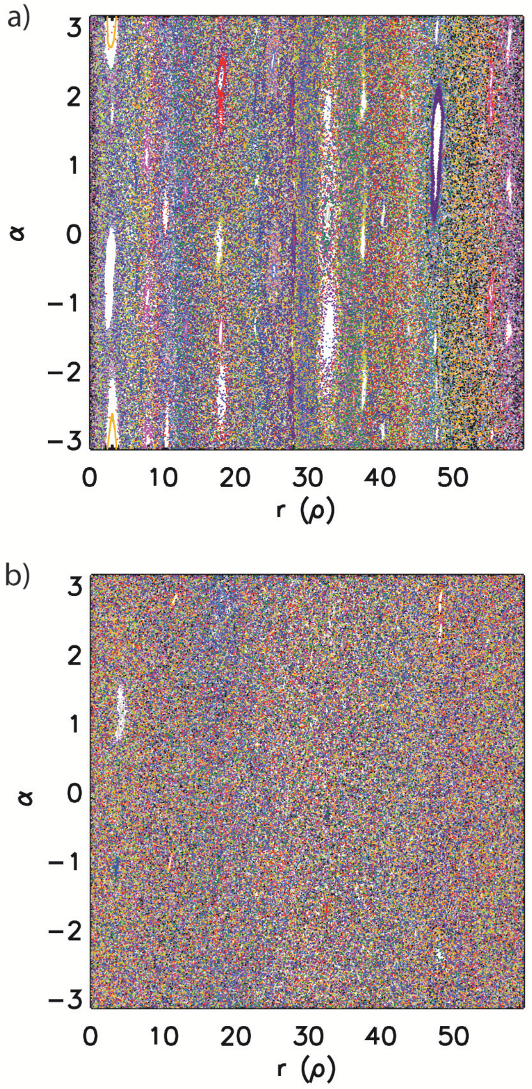

FIG. 3. (Color online) Poincaré map for $t = 450a/c_s$ demonstrating stochastic sea at a) $\beta_e = 0.1\%$ and b) $\beta_e = 0.7\%$

respectively. The crossing of Equation 12 with the $\beta_e = 0.1\%$ in Figure 4 indicates island overlap to occur for roughly $k_\perp \rho > .4$, and we see the last column of Figure 5a) does not produce widespread stochasticity. The intersection between Equation 12 and island width of $\beta_e = .7\%$ occurs for $k_\perp \rho > 0.2$, and we indeed see chaotic trajectories beginning with the second column of Figure 5 and fully developed in the third column. We conclude that the widespread stochasticity found in gyrokinetic simulations of CYCLONE parameters is necessarily a consequence of interaction of islands of differing order.

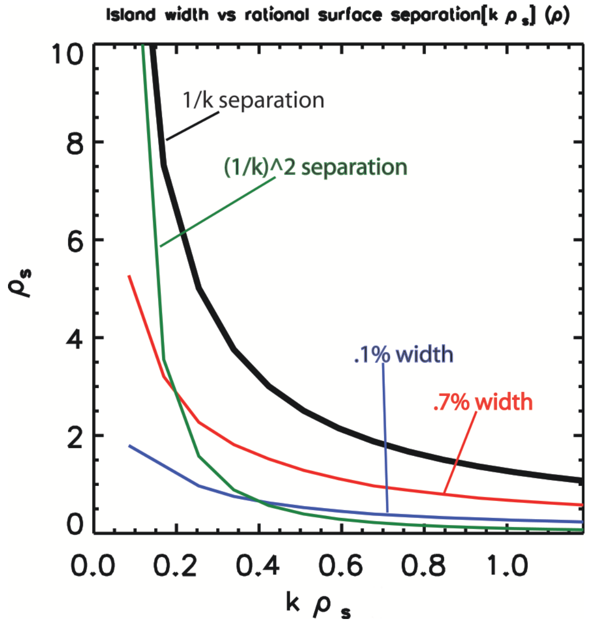

FIG. 4. (Color online) Rational surface separation for constant $k_\perp \rho_s$ (black) and neighboring modes (green) vs island width of $\beta_e = 0.7\%$ (red) and $\beta_e = 0.1\%$ (blue)

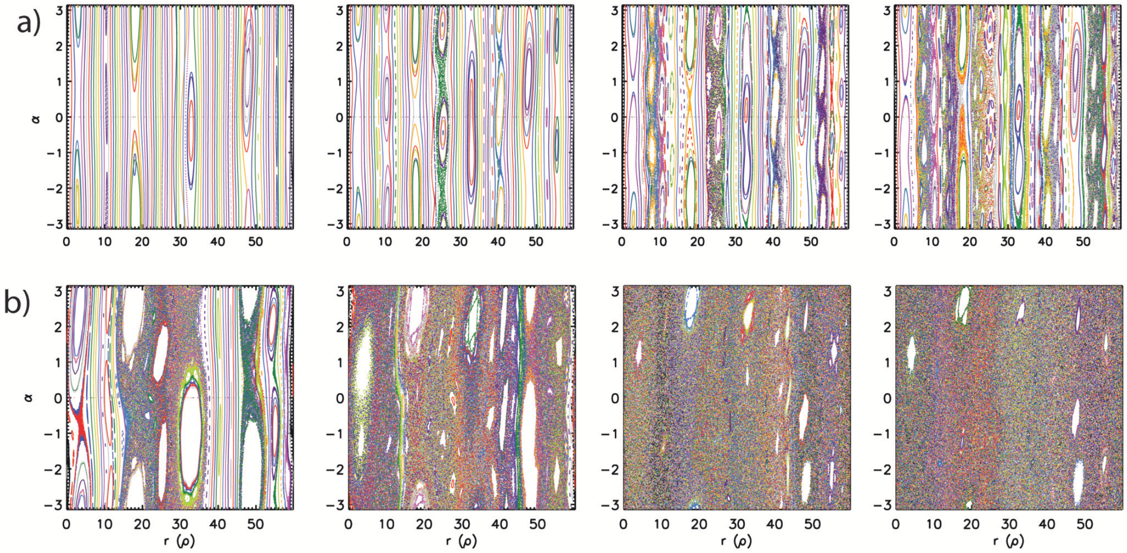

FIG. 5. (Color online) Poincaré plots for for $t = 450 c_s/a$ and a) $\beta_e = 0.1\%$ and b) $\beta_e = 0.7\%$, where an increasing number of toroidal modes are kept. The first column corresponds to the field trajectories of only $k_\perp \rho_s = 0.084$, second including $k_\perp \rho_s = 0.084$ and .168, third including $k_\perp \rho_s = 0.084, 0.168,$ and 0.252 and the last column $k_\perp \rho_s = 0.084, 0.168, 0.252$ and 0.336

QUANTIFYING TRANSPORT CAUSED BY STOCHASTIC FIELDS

The lack of electron heat transport despite evidence of widespread destruction of magnetic surfaces requires a nuanced interpretation of transport in chaotic fieldline trajectories. An intuitive way to start would be by considering the mean-squared radial displacement versus poloidal crossings. The magnetic diffusion coefficient [13], defined in Equation 13, is a means of quantifying the degree of stochasticity in the fields. Poincaré surface of section plots created in the previous section provide a direct method of calculating the magnetic diffusion coefficient d_m, given by

$$d_m = \lim_{\ell \to \infty} \frac{< [r_i(\ell) - r_i(0)]^2 >}{2\ell} \approx \lim_{\ell \to \infty} \frac{1}{2\ell} \frac{1}{N} \sum_{i=1}^{N} [r_i(\ell) - r_i(0)]^2 . \tag{13}$$

Note that d_m has units of length. In the last step of Equation 13, we have averaged over the 100 individual fieldlines followed in the plots. Figure 6 gives the magnetic diffusion coefficient for several independent time slices for $\beta_e = 0.7\%$. d_m is well estimated by taking the average value between 1500 and 3000 turns because the values trend to a constant, with variations over cycle number n_{cycle}, within a single time slice being significantly less than the variation between time slices. By producing surface of section plots at each time slice of of simulation, the time dependence of d_m can be calculated and compared to the time dependence of the electron heat flux observed in our simulations.

Reference [17] describes an exact relation between the magnetic diffusion coefficient d_m and associated electron heat flux Q_{st} in the collisionless limit, appropriate for the CYCLONE base case. However, we caution the reader in that Reference [17] assumes a relation between the ambipolar electric field, created from electrons diffusing by radial streaming relative to static ions, to the density and temperature gradients of the equilibrium to derive the equation below. It is far from clear that this assumption will be valid in a flux tube simulation where there is no average radial electric field, and a more rigorous connection between d_m and Q_{st} is the subject of ongoing investigation. Nevertheless, we present this model of stochastic heat transport, found between Equations 6 and 7 in [17] as a 'working model' for the energy flux.

$$Q_{st} = -2\sqrt{\frac{2}{\pi}} d_m v_{th} \left(\frac{\partial T}{\partial r} \right) (f_p n). \tag{14}$$

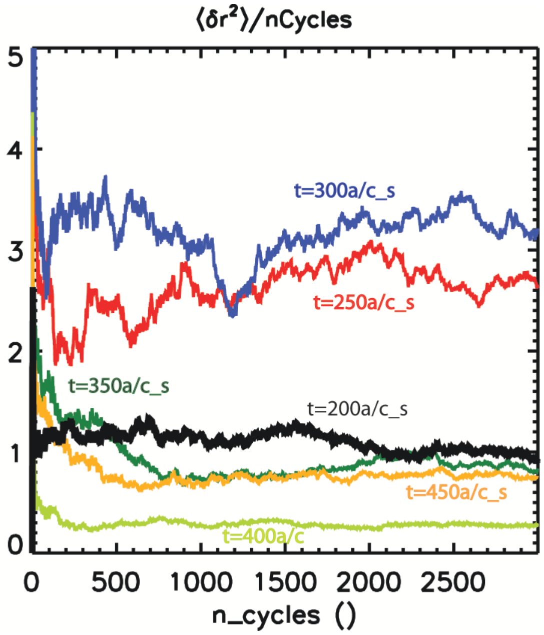

FIG. 6. (Color online) $d_m * (2 * 2\pi q R)$ as a function of turns around the tokamak for $\beta = .7\%$.

Above, $v_{th} = \sqrt{T/m}$ is the thermal velocity of the particle. To compare this to the transport output by GYRO, the density in Equation 14 is modified from the original reference in that it must be multiplied by the passing particle fraction ($f_p \approx 1 - \sqrt{\frac{r}{R}} \approx 55\%$ in CYCLONE) because trapped particles are confined about the outboard midplane and will not follow the stochastic fieldlines over long distances. The resulting stochastic electron heat flux is then obtained by combining Equations 13 and 14. Figure 7 shows the excellent agreement between the stochastic transport model and the actual output from GYRO in both magnitude and time behavior. Fig 8 shows this agreement over the range of the β_e scan.

Stochastic transport for microtearing unstable simulation

We conclude our analysis by applying the working model of stochastic transport to a nonlinear simulation where the magnetic component of electron transport consists of greater than 97% of the total transport in the simulation. The local simulation aims to model the NSTX discharge 120968, which is included in a set of confinement scaling experiments [18, 19]. The numerically reconstructed equilibrium is used as well as the measured physical parameters at $r/a = 0.6$, $T_i/T_e = 0.95$, $a/L_{Ni,Ne} = -0.83$, $a/L_{Ti} = 2.4$, $a/L_{Te} = 3.7$, $\mu = 60$,

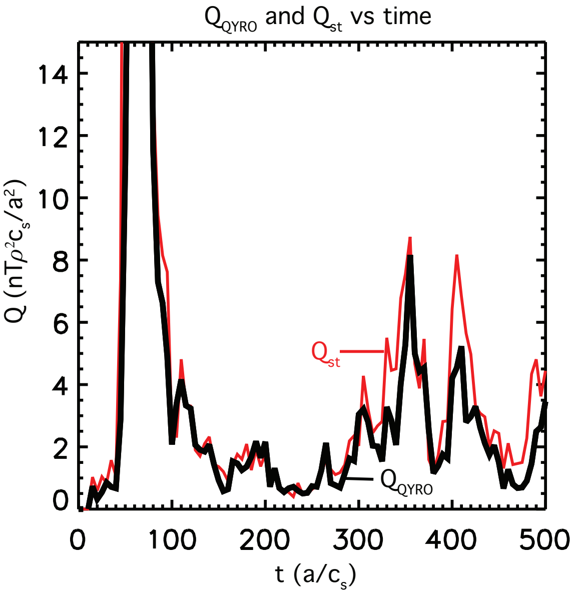

FIG. 7. (Color online) Stochastic heat transport Q_{GYRO} (black) and Q_{st} (red) vs time at $\beta_e = .7\%$

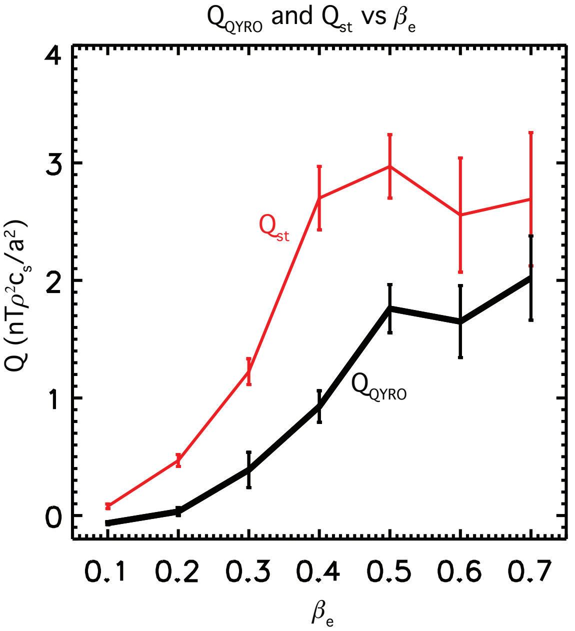

FIG. 8. (Color online) Stochastic heat transport Q_{GYRO} (black) and Q_{st}(red). Time averages were taken between $t = 150c_s/a$ and $t = 500c_s/a$. vs β_e.

$s = 1.7$, $\rho_* = 0.0075$, $q = 1.7$ and $\nu_{ei} = 1.46$. The spatial resolution includes 8 toroidal modes ($k_\perp = 0, 0.105, ..., 0.735$) and 400 radial gridpoints, while velocity space contains 192 points(8 energies, 12 pitch angles and 2 signs of velocity). At this radial location the only linear instability present is the microtearing mode, which has been observed previously in

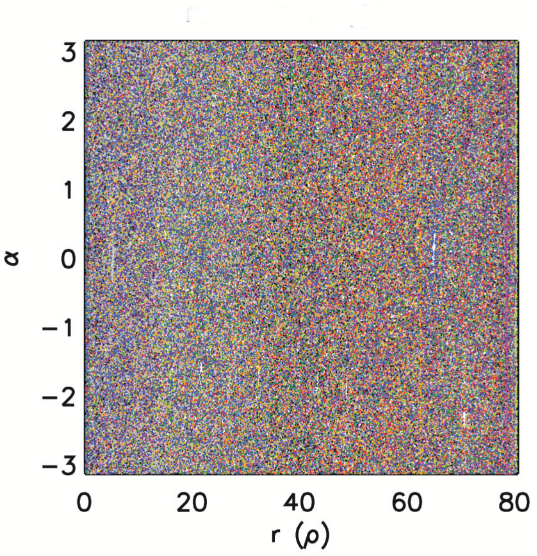

FIG. 9. (Color online) Representative Poincaré plot for simulation of NSTX shot 120968

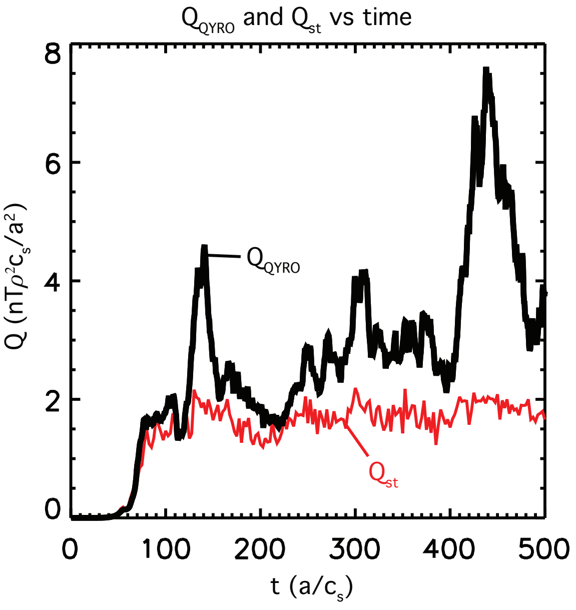

FIG. 10. (Color online) Q_{GYRO} (black) and Q_{st} (red) vs time in NSTX shot 120968

some spherical tokamak discharges [20–22].

This simulation contains a finite value of collisionality (required for the microtearing mode to be unstable), bringing into question whether Equation 14, which is produced in the collisionless limit, is the appropriate relation between d_m and Q_{st}. The electron mean free path is roughly 12.5 meters, while the stochastic correlation length [13, 14] $L_c = \pi R/\ln(.5\pi *$

$\hat{s}) \approx 2.5m$. Because the mean free path is significantly longer than the correlation length, the collisionless limit relating d_m and Q_{st} is still appropriate. As with CYCLONE, widespread stochasticity is observed (Figure 9). In this case, the amplitude of $A_\parallel$ is large enough so that the island width of $A_\parallel(n)$ is larger than the rational surface separation $1/k_\perp s$ for all but the lowest two toroidal modes. Figure 10 plots Q_{st} and the output heat flux from GYRO versus time. The stochastic heat transport model does an excellent job of predicting the baseline level of transport, but fails to describe bursts in transport, whose magnitude can be triple that of the baseline. The bursts in transport are caused individually by the lowest $k_\perp\rho$ modes in the system. To understand why the stochastic heat transport model fails to agree with the bursts in transport in Figure 10, we begin by noting

$$Q_{em} = \left\langle \int d^3v \frac{1}{2} m v^2 v_\parallel \frac{\delta B_r}{B_0} \delta f \right\rangle, \tag{15}$$

where $\langle A \rangle$ is the flux surface average of a quantity. In general, the drift kinetic equation would solve for the electron perturbed distribution function δf.

$$\frac{\partial \delta f}{\partial t} + v_\parallel \frac{\partial \delta f}{\partial \ell} + \left[v_\parallel \frac{\delta B_r}{B} + \frac{(\delta E \times B)_r}{B_0^2} \right] \frac{\partial f_0}{\partial r} + q v_\parallel E_\parallel \frac{\partial f_0}{\partial v_\parallel} = 0. \tag{16}$$

The stochastic transport model assumes parallel streaming is the dominant effect on perturbed electrons and consequently only keeps the second and third terms in Equation 16. Missing from the Rechester Rosenbluth treatment, but nonetheless potentially still of the same order are terms containing the perturbed electric field, high frequency perturbations and the response to the parallel electric field. Keeping only the second and third terms of Equation 16, we find the following solution for δf:

$$\delta f_{v_\parallel > 0}(\ell) = - \int_{-\infty}^{\ell} d\ell' \left[\frac{\delta B_r(\ell')}{B_0} \right] \frac{\partial f_0}{\partial r}. \tag{17}$$

$$\delta f_{v_\parallel < 0}(\ell) = + \int_{\ell}^{\infty} d\ell' \left[\frac{\delta B_r(\ell')}{B_0} \right] \frac{\partial f_0}{\partial r}. \tag{18}$$

Equations 17 and 18 are then used in Equation 15 to obtain the stochastic heat flux,

$$Q_{st} \approx d_m \int d^3v \frac{1}{2} m v^2 |v_\parallel| \frac{\partial F_0}{\partial r}, \tag{19}$$

where we used the fact that

$$d_m = \frac{1}{2\pi qR}\int_{-\pi qR}^{\pi qR} d\ell \int_{-\infty}^{\infty} d\ell' \frac{dB_r(\ell)dB_r(\ell')}{B_0^2}. \tag{20}$$

The definition of Equation 20 is equivalent to that given in Equation 13 above (see, for example, Reference [17]). The fact that the Rechester Rosenbluth model does so well in Figure 7, suggests that parallel streaming is the only imporant effect in electromagnetic electron heat transport for they CYCLONE base case, while the disagreement between Q_{st} and Q_{GYRO} indicates correlations between the vector potential and perturbed electric fieldcontribute to the bursts in electron electromagnetic transport. High frequency perturbations (where the $\partial f/\partial t$ term might be important) were not observed in these simulations.

Outside of stochastic transport, there are many interesting and important results arising from nonlinear simulations of the microtearing mode. A complete analysis of this simulation, including a parameter scan and interpretation of the results, and is left for a separate publication [23].

Conclusions

In the present paper, we have demonstrated magnetic reconnection and stochasticity occuring in gyrokinetic simulations of the CYCLONE base case when electromagnetic effects and kinetic electrons are included. The destruction of magnetic surfaces must be nonlinearly driven and is caused by interaction between islands of different order. The stochasticity does not necessarily correspond to an increase in electron heat flux, and is quantified by the magnetic diffusion coefficient. Although assumptions in the derivation are suspect for flux tube simulations, Reference [17] provides a working model to estimate the stochastic heat flux from d_m in the collisionless limit. By using the fraction of passing particles in Equation 14, the predicted stochastic heat flux is in excellent agreement with the output from GYRO in both time behavior and magnitude over the β_e scan. This estimate of stochastic energy transport is then applied to an experimentally relevant operating point where almost all of the transport is accounted by the magnetic component of electron transport. In this case, the stochastic transport model accurately predicts the baseline level of transport, but fails to describe intermittent bursts caused by the lowest modes in the system. In conclusion, the presented findings suggest that eradication of magnetic surfaces on the microscale could be a ubiquitous phenomenon. The electron heat transport associated with chaotic surfaces is well described by the magnetic diffusion coefficient d_m. A rigorous relation between d_m and Q_{st} and full analysis of the microtearing simulation are the subjects of ongoing research.

ACKNOWLEDGEMENTS

The authors gratefully acknowledge the National Center for Computational Sciences at ORNL for providing computer resources under INCITE award FUS023. We also acknowledge important conversations M.J. Puschel, who has also demonstrated that plasma microturubulence produces magnetic stochasticity over this beta scan using the GENE code. This work was performed under the auspices of the U.S. Department of Energy by Lawrence Livermore National Laboratory under Contract DE-AC52-07NA27344, by General Atomics under contract number DE-FG03-95ER54309 and by Princeton Plasma Physics Laboratory contract number DE-AC02-09CH11466.

---

[1] J. Candy and R.E. Waltz, J. Comput. Phys. **186**, 545 (2003).

[2] W. Dorland, F. Jenko, M. Kotschenreuther, and B.N. Rogers, Phys. Rev. Lett. **85**, 5579 (2000).

[3] Y. Chen and S. Parker, J. Comput. Phys. **189**, 463 (2003).

[4] A.G. Peeters, Y. Camenen, F.J. Casson, W.A. Hornsby, A.P. Snodin, D. Strintzi, and G. Szepesi, Computer Physics Communications **180**, 2650 (2009).

[5] J. Candy, Phys. Plasmas **12**, 072307 (2005).

[6] M. J. Pueschel, M. Kammerer, and F. Jenko, Phys. Plasmas **15**, 102310 (2008)

[7] A.M. Dimits, G. Bateman, M.A. Beer, B.I. Cohen, W. Dorland, G.W. Hammett, C. Kim, J.E. Kinsey, M. Kotschenreuther, A.H. Kritz, L.L. Lao, J. Mandrekas, W.M. Nevins, S.E. Parker, A.J. Redd, D.E Schumaker, R. Sydora, and J. Weiland, Phys. Plasmas **7**, 969 (2000).

[8] R. E. Waltz, Phys. Plasmas **17**, 072501 (2010)

[9] M. J. Pueschel, and F. Jenko, Phys. Plasmas **17**, 062307 (2010)

[10] J.Y. Kim, W. Horton, and J.Q. Dong, Phys. Fluids B **5** (11), 4030 (November, 1993).

[11] M.D. Kruskal and R.M. Kulsrud, Phys. fluids, 1:265, 1958

[12] W.M. Nevins, E. Wang, and J. Candy, Phys. Rev. Lett. **106**, (Feb. 11, 2011)

[13] A.B. Rechester and M.N. Rosenbluth, Phys. Rev. Lett. **40**, 38 (1978).

[14] G.M. Zaslavsky and B.v. Chirikov, Sov. Phys. Usp. **14**, 549 (1972).

[15] A.H. Reiman and D.A. Monticello, Nucl. Fusion **32** 1341 (1992).

[16] D.R. Hatch, P.W. Terry, F. Jenko, F. Merz, M.J. Pueschel, W.M. Nevins, E. Wang, "Role of subdoimant modes in plasma microturbulence", submitted to Phys. Plasmas.

[17] R. W. Harvey, M. G. McCoy, J. Y. Hsu, and A. A. Mirin, Phys. Rev. Lett. **47**, 102105 (1981).

[18] S.M. Kaye, R.E. Bell, D. Gates, B.P. LeBlanc, F.M. Levinton, J.E. Menard, D. Mueller, G. Rewoldt, S.A. Sabbagh, W. Wang, and H. Yuh, Phys. Rev. Lett. **98**, 175002 (2007).

[19] S.M. Kaye, F.M. Levinton, D. Stutman, K. Tritz, H. Yuh, M.G. Bell, R.E. Bell, C.W. Domier, D. Gates, W. Horton, J. Kim, B.P. LeBlanc, N.C. Luhmann Jr, R. Maingi, E. Mazzucato, J.E. Menard, D. Mikkelsen, D. Mueller, H. Park, G. Rewoldt, S.A. Sabbagh, D.R. Smith, and W. Wang, Nucl. Fusion **47**, 499 (2007).

[20] D. J. Applegate, C. M. Roach, J. W. Connor, S. C. Cowley, W. Dorland, R. J. Hastie, and N. Joiner, Plasma Phys. Control. Fusion **49**, 1113 (2007).

[21] K. L. Wong, S. Kaye, D. R. Mikkelsen, J. A. Krommes, K. Hill, R. Bell, and B. LeBlanc, Phys. Rev. Lett. **99**, 135003 (2007)

[22] K. L. Wong, S. Kaye, D. R. Mikkelsen, J. A. Krommes, K. Hill, R. Bell, and B. LeBlanc, Phys. Plasmas **15**, 056108 (2008).

[23] W. Guttenfelder et al., submitted to Phys. Rev. Lett. Dec 2011